Periocular Recognition by Detection of Local Symmetry Patterns

Anna Mikaelyan, Fernando Alonso-Fernandez, Josef Bigun
School of Information Science, Computer and Electrical Engineering
Halmstad University
Box 823. SE 301-18 Halmstad, Sweden.
Email: {annmik, feralo, josef.bigun}@hh.se

***Abstract*—We present a new system for biometric recognition using periocular images. The feature extraction method employed describes neighborhoods around keypoints by projection onto harmonic functions which estimates the presence of a series of various symmetric curve families around such keypoints. The iso-curves of such functions are highly symmetric w.r.t. the keypoints and the estimated coefficients have well defined geometric interpretations. The descriptors used are referred to as Symmetry Assessment by Feature Expansion (SAFE). Extraction is done across a set of discrete points of the image, uniformly distributed in a rectangular-shaped grid positioned in the eye center. Experiments are done with two databases of iris data, one acquired with a close-up iris camera, and another in visible light with a webcam. The two databases have been annotated manually, meaning that the radius and center of the pupil and sclera circles are available, which are used as input for the experiments. Results show that this new system has a performance comparable with other periocular recognition approaches. We particularly carry out comparative experiments with another periocular system based on Gabor features extracted from the same set of grid points, with the fusion of the two systems resulting in an improved performance. We also evaluate an iris texture matcher, providing fusion results with the periocular systems as well.**

***Index Terms*—Biometrics, periocular recognition, eye, symmetry filters, structure tensor**

I. Introduction

Periocular recognition has gained attention recently in the biometrics field [1], [2], [3] with some pioneering works already in 2002 [4] (although authors here did not call the local eye area 'periocular'). Periocular refers to the face region in the immediate vicinity of the eye, including the eye, eyelids, lashes and eyebrows. While face and irises have been extensively studied [5], [6], the periocular region has emerged as a promising trait for unconstrained biometrics, following demands for increased robustness of face or iris systems. With a surprisingly high discrimination ability [1], this region can be easily obtained with existing setups for face and iris, and the requirement of user cooperation can be relaxed. It has also another advantages, such as its availability over a wide range of distances even when the iris texture cannot be reliably obtained (low resolution) or under partial face occlusion (close distances). Most face systems use a holistic approach, requiring a full face image, so the performance is negatively affected in case of occlusion [2]. Periocular region has also shown to have superior performance than face under extreme values of blur or down-sampling [7]. This points out the strength of periocular recognition when only partial face images are available, for example forensics or surveillance cameras, or in more relaxed scenarios such as distant acquisition or mobile devices. In addition, the periocular region appears in iris images, so fusion with the iris texture has potential to improve the overall recognition [8], [9]. In most of the existing studies, images have been acquired in the visible range [1]. Periocular on visible light works better than on near-infrared (NIR), because it shows melanin-related differences [3]. On the other hand, many iris systems work with NIR illumination due to higher reflectivity of the iris tissue in this range [10]. Unfortunately, the use of more relaxed scenarios will make NIR light unfeasible (e.g. distant acquisition, mobile devices) so there is a high pressure to the development of algorithms capable of working with visible light.

An overview of existing approaches for periocular recognition is given in [1]. The most widely used approaches include Local Binary Patterns (LBP) [11] and, to a lesser extent, Histogram of Oriented Gradients (HOG) [12] and Scale-Invariant Feature Transform (SIFT) keypoints [13]. The use of different experimental setups and databases make difficult a direct comparison between existing works. The study of Park *et al*. [2] compares LBP, HOG and SIFT using the same data, with SIFT giving the best performance (rank-one recognition accuracy: 79.49%, EER: 6.95%), followed by LBP (rank-one: 72.45%, EER: 19.26%) and HOG (rank-one: 66.64%, EER: 21.78%). Other works with LBPs, however, report rank-one accuracies above 90% and EER rates below 1% [14], [15], [8]. Gabor features were also proposed in a seminal work of 2002 [4], although this work did not call the local eye area 'periocular'. Here, the authors used three machine experts to process Gabor features extracted from the facial regions surrounding the eyes and the mouth, achieving very low error rates (EER$\leq$0.3%). This system served as inspiration for a Gabor-based periocular system that we proposed in [16] (used in the experiments of this paper). Another important set of research works have concentrated their efforts in the fusion of different algorithms. For example, Bharadwaj *et al*. [17] fused Uniform LBPs (ULBP) with a global descriptor (GIST) consisting of perceptual dimensions related with scene description (image naturalness, openness, roughness, expansion and

ruggedness). The best result, obtained by the fusion of both systems, was a rank-one accuracy of 73.65%. Juefei-Xu *et al*. [18], [19] fused LBP and SIFT with other local and global feature extractors including Walsh masks [20], Laws Masks [21], DCT [22], DWT [23], Force Fields [24], SURF [25], Gabor filters [26], and Laplacian of Gaussian. The best result obtained was a rank-one accuracy of 53.2% by fusion of DWT and LBP. Finally, Hollingsworth *et al*. [3] evaluated the ability of (untrained) human observers to compare pairs of periocular images, resulting in a rank-one accuracy of 88.4% (VW data) and 78.8% (NIR data).

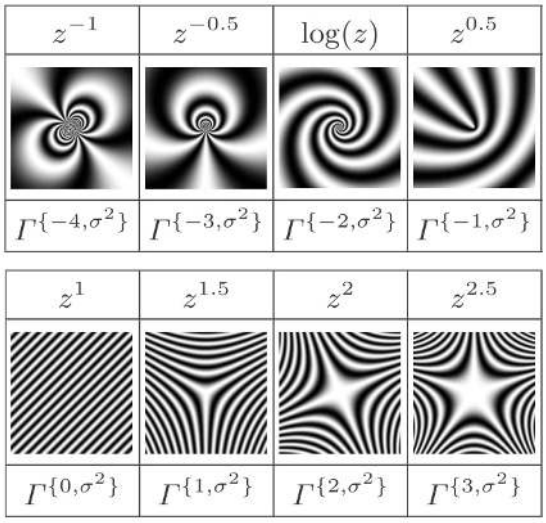

Fig. 1. Example of families of symmetric patterns. Top row of each subplot: analytic function $q(z)$ used to generate each pattern. Bottom row of each subplot: symmetry derivative filter Γ^{n,σ^2} of order n suitable to detect the pattern family.

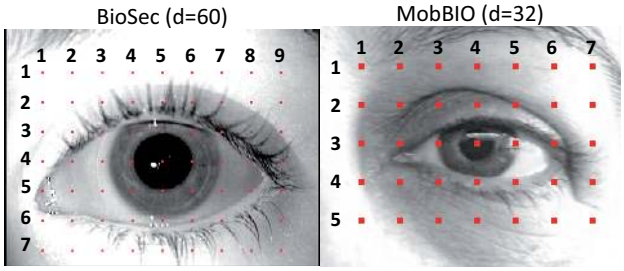

Fig. 2. Sampling grid configuration. Parameter d indicates the horizontal/vertical distance between adjacent points.

In this paper, we propose a new periocular recognition system based on a systematic series of structure tensors in curvilinear coordinates, which estimates the spatially varying orientation by projection onto harmonic functions. This encodes the presence of a series of various symmetric curve families (Figure 1) around keypoints. Features are extracted in a set of discrete points (pixels) only, uniformly distributed across the image in a rectangular-shaped sampling grid which is centered in the pupil (Figure 2). The functions share a singularity at their origin, defining the location of keypoints precisely, whereby they describe the object properties of neighborhoods. Energies of the features measure object properties which are concentrated to a point by design. This is novel and complementary to traditional texture features which are purposively invariant to translation (within a texture). The features used are called Symmetry Assessment by Finite Expansion (SAFE), which we have recently proposed and used for forensic fingerprint recognition [27].

We use two iris databases, one with close-up NIR data and another with webcam (visible) data. Our system achieves competitive verification rates with respect to existing periocular approaches. We carry out direct comparison with another periocular system based on Gabor texture features [16], showing that the fusion of the two systems can achieve better performance (up to 14% of improvement in the EER has been observed). We also evaluate an iris texture matcher based on 1D Log-Gabor wavelets. Despite the performance of this matcher is considerably lower with the webcam database, we observe an interesting complementarity with the periocular modality under this type of images, with performance improvements of more than 40% with the fusion of the iris matcher and any of the periocular systems.

II. System Description

Our recognition system is based on the SAFE features proposed in [27] for forensic fingerprint recognition. We start by extracting the complex orientation map of the image (Figure 3) [28]. We then project ring-shaped areas of different radii around selected keypoints onto an space of harmonic functions [29]. By keeping the number of basis and rings low, the extracted features are low dimensional. The system is described in detail next.

A. The Generalized Structure Tensor (GST) and the Linear Symmetry Tensor (LST)

The Generalized Structure Tensor (GST) has been introduced as a tool for symmetry detection [29]. The GST represents a pair of functions $(I20^{(n)}, I11^{(n)})$ which are result of nonlinear operations between an image f and the n-th symmetry derivative of a Gaussian, Γ^{n,σ^2}:

$$GST(n) = (I20^{(n)}, I11^{(n)}) = \\ (\Gamma^{n,\sigma_2^2} * (\Gamma^{1,\sigma_1^2} * f)^2, |\Gamma^{n,\sigma_2^2}| * |\Gamma^{1,\sigma_1^2} * f|^2) \quad (1)$$

with

$$\Gamma^{n,\sigma^2} = r^n \frac{1}{2\pi\sigma^2} e^{-\frac{r^2}{2\sigma^2}} e^{in\varphi}, \text{ being } r = |x+iy|. \quad (2)$$

The main use of the GST is the detection of position and orientation of symmetric patterns such as lines, circles, parabolas, etc., as those shown in Figure 1. Symmetric patterns are generated by harmonic function pairs $\xi(x,y)$ and $\eta(x,y)$ with iso-curves of ξ and η being locally orthogonal to each other [30]. These harmonic function pairs can be easily obtained as the real and imaginary parts of any analytic function $q(z)$, with $z = x + iy$. For example, the

symmetric patterns of Figure 1 are generated by using the 1D equation $(-\xi \sin\theta + \eta \cos\theta) = constant$. The top row indicates the analytic function used to generated each pattern, while the bottom row indicates the order of the symmetry derivative of gaussian (indexed by n) suitable to detect the pattern family by means of Equation 1. The iso-curves of the patterns are parallel lines in curvilinear coordinate system (given by the two harmonic basis curves ξ and η) and they reverse to parabola, circle, spiral, etc. when transformed to Cartesian coordinates. The beauty of this method is that these transformations are not applied to the input image, but they are implicitly encoded in the utilized complex filters, so detection of such intricate patterns is done directly in Cartesian coordinates, as per Equation 1. The parameter θ controls the orientation of the symmetric pattern (except for $q(z) = \log(z)$) and changing the pair ξ, η results in a completely different family of patterns. It can be demonstrated from the triangle inequality that $|I20^{(n)}| \leq I11^{(n)}$, so $I11^{(n)}$ is normally used for normalizing values of $I20^{(n)}$ to be scale invariant for any n:

$$\frac{\left|I20^{(n)}\right|}{I11^{(n)}} \leq 1 \tag{3}$$

Thus, the image $\left|I20^{(n)}\right| / I11^{(n)}$ gives evidence/certainty of a specific symmetry type in f (with location given by local maxima) and the orientation of the pattern is encoded in the argument $\angle I20^{(n)}$ (in double angle). The latter is also important, since one unique filter detects a whole family of patterns regardless of the orientation of the pattern. Equality in Equation 3 holds in case of strong directional dominance (i.e. presence) of the corresponding pattern. For Cartesian coordinate space, $\xi = x$ and $\eta = y$, the GST evaluates the direction in which most of the energy is concentrated, i.e. linear symmetry. This corresponds to the local orientation of the image, and it is referred as the Linear Symmetry Tensor (LST) [28]:

$$LST = (I20^{(0)}, I11^{(0)}) \triangleq GST(0) \tag{4}$$

The argument of complex pixel values of $I20^{(0)}$ encodes the local orientation of the image (in double angle), and values of $I11^{(0)}$ measure the strength, which is used to normalize values of $I20^{(0)}$, according to Equation 3.

B. Feature Extraction by Projection on Harmonic Functions

The complex image $I20^{(n)}$ can also be obtained as:

$$I20^{(n)} = \Gamma^{n,\sigma_2^2} * I20^{(0)} \tag{5}$$

meaning that the image $I20^{(n)}$ used to detect the particular pattern given by n can be viewed as a scalar product between the orientation image $I20^{(0)}$ and the corresponding symmetry derivative filter Γ^{n,σ^2}. The parameter σ_1 in Equation 1 defines the derivation filters in the computation of the orientation image (determined by the estimated noise level), whereas σ_2, used in the computation of $I20^{(n)}$ and $I11^{(n)}$, defines the size extension of the sought pattern. This makes Γ^{n,σ^2} a projection basis for a Hilbert space [31], which is achieved here by choosing the spatial supports of Γ^{n,σ^2} in radially disjoint regions defined by concentric annular rings. Every annulus is constructed by means of a derivative of a Gaussian, using a modified version of Equation 2:

$$\psi_{mk} = (1/\kappa_k) r^n e^{-\frac{r}{2\sigma^2}} e^{im\varphi}. \tag{6}$$

Here, ψ_{mk} is identical to Γ^{n,σ^2} except that $\|\psi_{mk}\| = 1$ is ensured via the normalization constant κ_k, and that the exponent of r^n is now a constant n (which defines the width of the filter), independent of the symmetry order (which is now called m). The position of the filter peak is controlled by σ via $r_k = \sqrt{n}\sigma$, with r_k being the desired position of the peak. In other words, we can tune the filters to be used by the GST to work on a desired annular band of the image, with known radius and width, via Equation 6. For feature extraction, we define a range of radii $[r_{min}, r_{max}]$, and build N_f filters with peaks log-equidistantly sampled in this range (Figure 4). The filters are normalized (via $\|\psi_{mk}\| = 1$) to have an underlying area of the same size, so that the value of extracted features is independent of the annuli size. We therefore extract image information at N_f annular rings of different radii r_k ($k = 1...N_f$).

According to Equation 5, the feature extractor requires as input the complex orientation image. We extract annular rings from the orientation image around selected keypoints as:

$$f_k = \frac{I20^{(0)}}{I11^{(0)}} |\psi_{mk}| \tag{7}$$

Keypoints are selected on the basis of an sparse retinotopic sampling grid positioned in the center of the eye (Figure 2). The grid has rectangular geometry, with sampling points distributed uniformly. We use a relative low dense grid, to keep the size of the feature set small, and to allow faster processing. This grid is inspired by other periocular works [9], where it is also demonstrated that more dense grids do not necessarily lead to better performance. Feature extraction is thus made in the points of the grid in an analogue way as Equation 1, but with the orientation image $I20^{(0)}/I11^{(0)}$ now confined to a ring:

$$I20^{(m)} = < \psi_{mk}, f_k > = < |\psi_{mk}|^2 e^{im\varphi}, \frac{I20^{(0)}}{I11^{(0)}} > \tag{8}$$

$$I11^{(m)} = < |\psi_{mk}|, |f_k| > = < |\psi_{mk}|^2, \frac{|I20^{(0)}|}{I11^{(0)}} > \tag{9}$$

Therefore, we use the result of scalar products of harmonic filters ψ_{mk} with the orientation image neighborhood around keypoints to quantify the amount of presence of pattern families as those shown in Figure 1 in annular rings around each keypoint (with order of the symmetric pattern given by m). The feature vector dimension describing a keypoint is given by the number of rings (N_f) and the size of the projection base (N_h) inside each ring, leading to $N_f \times N_h$ features

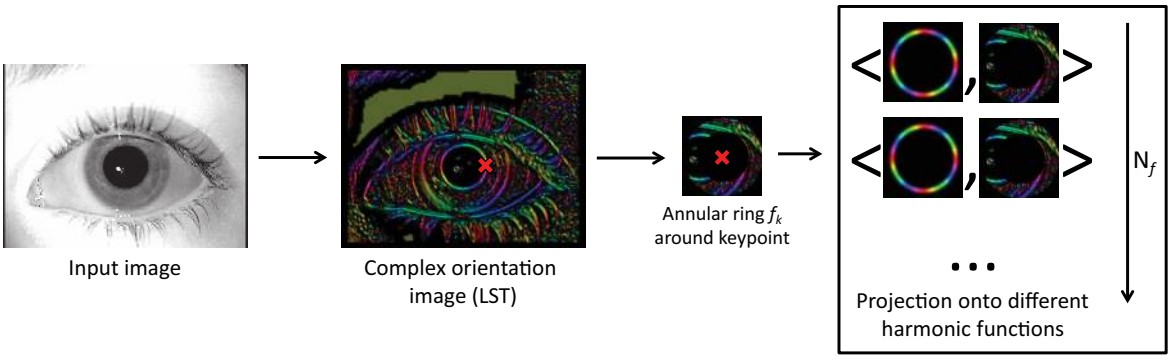

Fig. 3. Feature extraction process for one filter radius. The hue encodes the direction, and the saturation represent the complex magnitude.

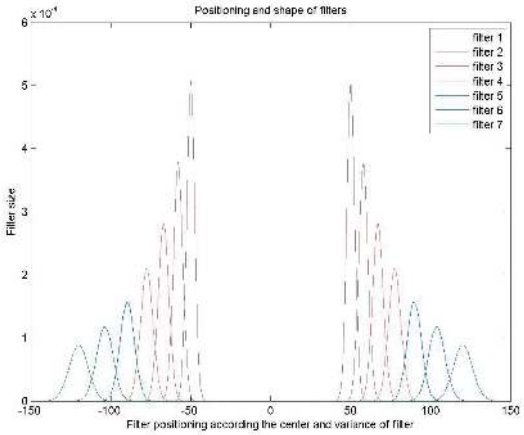

Fig. 4. Cross-section of annular filters ($N_f = 7$).

for each sampling point. In this work, we employ $N_f = 9$ annular regions and $N_h = 9$ different families symmetries (from $m = -4$ to 4). As it follows from the triangle inequality, the extracted features are normalized as:

$$SAFE_{mk} = \frac{I20^{(m)}}{I11^{(m)}} \in \mathbb{C}, \text{ with } |SAFE_{mk}| \leq 1 \qquad (10)$$

and all features computed in a keypoint are put together in a complex array $\mathbf{SAFE}$ of $N_f \times N_h$ elements. The suggested $SAFE_{mk}$ features are complex-valued and their magnitudes represent the amount of reliable orientation field within the annular ring k explained by the $m-th$ symmetry basis, with $SAFE_{mk} = 1$ being full explanation.

C. Matching

To match two complex-valued feature vectors $\mathbf{SAFE}^r$ and $\mathbf{SAFE}^t$, we use again the triangle inequality:

$$M = \frac{< \mathbf{SAFE}^r, \mathbf{SAFE}^t >}{< |\mathbf{SAFE}^r|, |\mathbf{SAFE}^t| >} \in \mathbb{C} \qquad (11)$$

The argument $\angle M$ represents the angle between $\mathbf{SAFE}^r$ and $\mathbf{SAFE}^t$ (which is expected to be zero when symmetry patterns detected by GST coincide for reference and test feature vectors, and 180° when they are orthogonal). The confidence of measure is given by $|M|$. To include confidence into the measured angle difference, we use the projection of angle:

$$MS = |M| \cos \angle M \qquad (12)$$

The resulting matching score $MS \in [-1, 1]$ and is equal to 1 for coinciding symmetry patterns in the reference and test vectors (full match). Low or zero certainty ($MS \simeq 0$) happens when the certainties in one of the respective descriptor components (their magnitudes) are zero, because of low quality data in annular rings or if the orientation data of reliable sectors of annular rings cannot be explained by the respective symmetric patterns. Full miss-match, or $MS = -1$, happens when reliable sectors (having $|M| = 1$) of all components between reference and test feature vectors point at symmetry patterns that are locally orthogonal. Matching between two images is done by computing the matching score MS between corresponding points of the sampling grid. All matching scores are then averaging, resulting in a single matching score between two given images.

III. Baseline Periocular and Iris Systems

The algorithm presented here is compared with the periocular system proposed in [16]. It makes use of the same sampling grid shown in Figure 2, so features are extracted from the same keypoints. The local power spectrum of the image is sampled at each point of the grid by a set of Gabor filters organized in 5 frequency channels and 6 equally spaced orientation channels. The Gabor responses from all points of the grid are grouped into a single complex vector, which is used as identity model. Matching between two images is using the magnitude of complex values. Prior to matching with magnitude vectors, they are normalized to a probability distribution (PDF), and matching is done using the χ^2 distance [32]. Due to different image size (see Section IV), Gabor filter wavelengths span from 4 to 16 pixels with the MobBIO database and 16 to 60 with BioSec. This covers approximately the range of pupil radius of each database, as given by the groundtruth.

We also conduct matching experiments of iris texture using 1D log-Gabor filters [33]. The iris region is unwrapped to a normalized rectangle using the Daugman's rubber sheet model [10] and next, a 1D Log-Gabor wavelet is applied plus phase binary quantization to 4 levels. Matching between binary vectors is done using the normalized Hamming distance [10], which incorporates the noise mask, so only significant bits are used in computing the Hamming distance. Rotation is accounted for by shifting the grid of the query image in counter- and clock-wise directions, and selecting the lowest distance, which corresponds to the best match between two templates.

Fig. 5. Example of images of the BioSec database with the annotated circles modeling iris boundaries and eyelids.

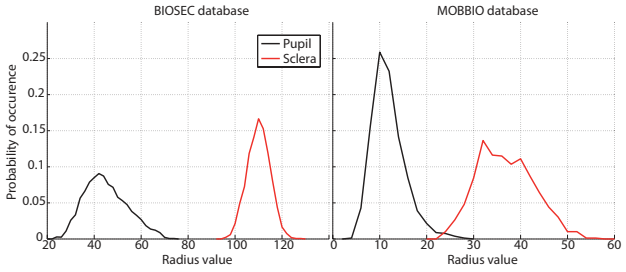

Fig. 6. Histogram of pupil and sclera radii of the two databases used here, as given by the groundtruth [34].

IV. Databases and Experimental Protocol

We use the BioSec [35] and MobBIO [36] databases. From BioSec, we select 1,200 images from 75 individuals acquired in 2 sessions (4 images of each eye per person, per session). Images are of 480×640 pixels, acquired with a LG IrisAccess EOU3000 close-up infrared iris camera. MobBIO has been captured with the Asus Eee Pad Transformer TE300T Tablet (a webcam in visible light) in one session. Images in MobBIO were captured in two different lightning conditions, with variable eye orientations and occlusion levels, resulting in a large variability of acquisition conditions. Distance to the camera was kept constant, however. From MobBIO, we use 800 iris images of 200×240 pixels from 100 individuals (4 images of each eye per person). The two databases have been annotated manually by an operator [34], meaning that the radius and center of the pupil and sclera circles are available, which are used as input for the experiments. Similarly, the eyelids are modeled as circles, which are used to build the noise mask of the iris matcher. Examples of annotated images are shown in Figure 5.

We carry out verification experiments. We consider each eye as a different user (200 available users in MobBIO, 150 in BioSec). Experiments with MobBIO are as follows. Genuine matches are done by comparing each image of a user to his/her remaining images, avoiding symmetric matches. Impostor matches are obtained by comparing the 1^{st} image of a user to the 2^{nd} image of the remaining users. We then get 200×6=1,200 genuine and 200×199=39,800 impostor matchings. With BioSec, genuine matches for a given user are obtained by comparing all images of the 1^{st} session to all images of the 2^{nd} session. Impostor matches are obtained by comparing the 2^{nd} image of the 1^{st} session of a user to the 2^{nd} image of the 2^{nd} session of the remaining users. We then obtain 150×4×4=2,400 genuine and 150×149=22,359 impostor matchings. Note that experiments with BioSec are made by matching images of different sessions, but these inter-session experiments are not possible with MobBIO.

Some fusion experiments are also done between different matchers. The fused distance is computed as the mean value of the distances due to the individual matchers, which are first normalized to be similarity scores in the $[0,1]$ range using tanh-estimators as $s' = \frac{1}{2}\left\{\tanh\left(0.01\left(\frac{s-\mu_s}{\sigma_s}\right)\right)+1\right\}$. Here, s is the raw similarity score, s' denotes the normalized similarity score, and μ_s and σ_s are respectively the estimated mean and standard deviation of the genuine score distribution [37].

V. Results

The performance of the periocular system proposed based on SAFE features is given in Figure 7 (top). We also provide results of the baseline periocular and iris matchers, as well as of different fusion combinations (bottom). The corresponding EERs are given in Table I. We test different range of radii of the symmetry filters based on the groundtruth information (Figure 6). For Mobbio, the smallest filter radius is set to 5 or 10, which is in proportion to the average radius of the pupil (around 10). Similarly, the biggest filter radius is set to 32 or 64, in proportion to the average radius of the sclera (around 32). This leads to the different combinations shown ('5-32', etc.). A similar reasoning is applied with Biosec: smallest filter radius proportional to 30 (average pupil radius), and biggest filter radius proportional to 100 (slightly smaller than the average sclera radius). This leads to the combinations '15-100' and '30-200'. For comparative reasons, we have also used with Biosec a range of radii comparable with those used with Mobbio, i.e.: '5-30', '5-60', and '10-60'. An example of these different configurations can be seen in Figure 8.

With Biosec (Figure 7 top, left), we observe that the different filter configurations have approximately the same performance. The best configuration corresponds to '5-60'. Only when the top-end of the range of radii is made large in comparison with the iris size (i.e. '30-200'), the performance shows a little worsening. This is in contrast with Mobbio, where the best configuration is the one covering as much as twice the average sclera radius (i.e. '10-64'). Decreasing the top-end of the radii here results in an appreciable worsening in performance (see '5-32'). It is worth highlighting that the optimum range of filter radii is quite similar for both databases,

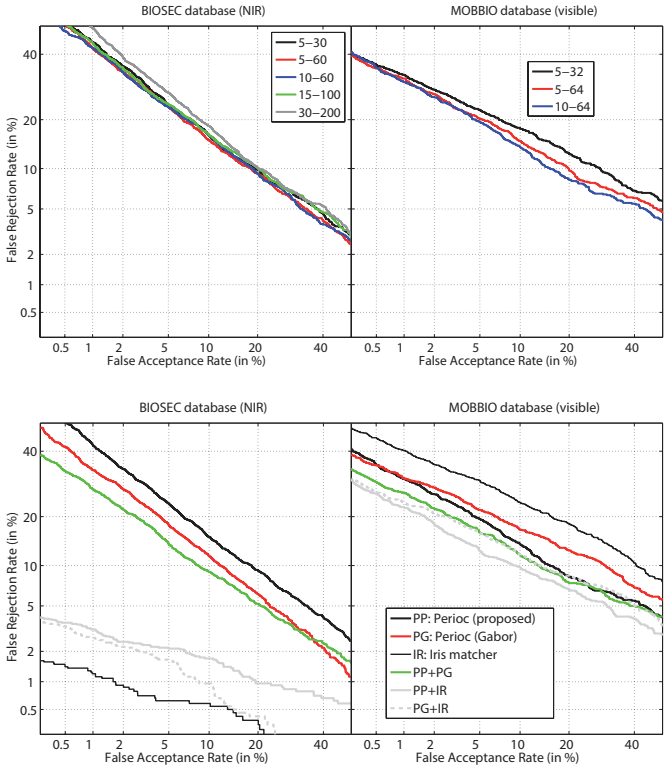

Fig. 7. **Top:** Performance of the periocular system proposed based on SAFE features for different configurations of the filters. **Bottom:** Comparison with the baseline periocular and iris matchers. The PP configurations employed in the bottom plot are the ones giving the best EER ('5-60' with Biosec, '10-64' with Mobbio).

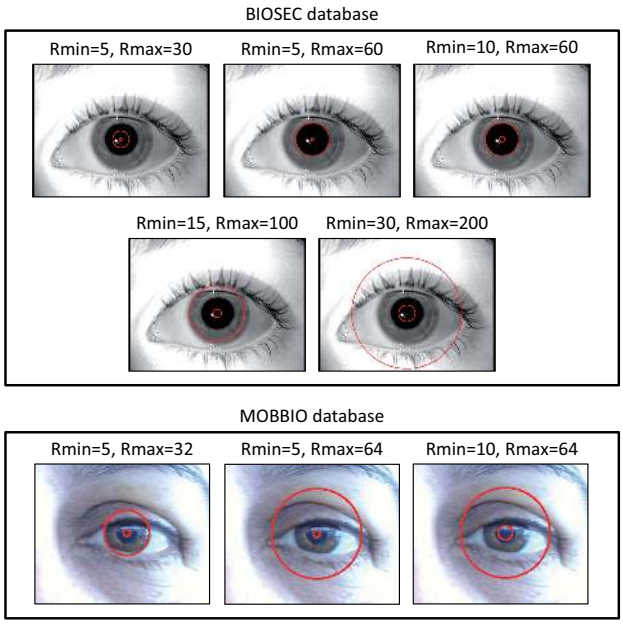

Fig. 8. Different configurations of the smallest and largest radii of the symmetry filters (examples are shown for the grid point situated in the center of the pupil).

despite different image size and illumination. These are also good news in the sense that the size of the filters of Equation 6 can be kept low even with bigger iris images, leading to computational savings during the convolutions of Equations 8 and 9.

As regards to differences between the two databases, the proposed system achieves better performance with Mobbio (EER of 11.96% vs. 12.81%). On the contrary, the baseline periocular system (labeled 'PG' in Figure 7 and Table I) shows opposite behavior. This can suggest that one feature is better than the other for a particular type of illumination used in the acquisition, but this is difficult to assess given the different image size. Different systems configurations than the ones used here may lead to different results. What is relevant however, is that Mobbio uses approximately half of the sampling points than Biosec (35 vs. 63, see Figure 2), but the performance of the periocular systems are not necessarily worse. The two periocular systems are also observed to be complementary, with the fusion ('PP+PG') resulting in up to 14% of EER improvement in both databases.

With respect to the iris matcher, its performance is much better in BioSec than in MobBIO, which is expected, since iris systems usually work better in NIR range [10]. An additional factor could be the differences in image size, and the worse acquisition conditions of MobBIO. It is worth noting that the periocular systems work better than the iris matcher in MobBIO. The smaller image size makes more difficult to reliably extract identity information for the iris texture. In this situation, the periocular region is still able to provide a rich source of identity. But even in the adverse acquisition conditions of MobBIO, the iris system is able to complement the periocular systems, as shown in the fusion results (with improvements in performance of more than 40%). This complementarity between the iris and periocular matchers is not observed in Biosec. The latter, however, should not be taken as a general statement. Other fusion rules may lead to different results with BioSec, specially if the supervisor is data quality and/or expert adaptive [38], [37]. Additional optimizations of the periocular systems towards smaller error rates can be another avenue to overcome this issue.

VI. Conclusions

A new periocular recognition system based on detection of local symmetry patterns is proposed. It is based on projecting ring-shaped areas of different radii around selected keypoints onto an space of harmonic functions which are tuned to detect various symmetric curve families [29]. Extracted features therefore quantify the presence of pattern families (Figure 1) in annular rings around each keypoint. The proposed features are called Symmetry Assessment by Finite Expansion (SAFE), which we have recently used for forensic fingerprint recognition [27]. Keypoints are selected on the basis of a sparse sampling grid positioned in the eye center, having rectangular geometry, with sampling points uniformly distributed across the image. The system is evaluated with two databases of iris data, one acquired with a close-up NIR camera, and another

BIOSEC database (NIR)

smallest filter	largest filter	Periocular			Iris	Periocular+Iris	
		Proposed (PP)	Gabor (PG)	Fusion PP+PG	IR	Fusion PP+IR	Fusion PG+IR
5	30	13.07	10.77	9.35 (-13.20%)	1.12	2.57	2.16
5	60	**12.81**		**9.28** (-13.87%)		2.40	
10	60	13.12		9.44 (-12.33%)		2.41	
15	100	13.47		9.82 (-8.84%)		2.40	
30	200	13.96		9.89 (-8.21%)		2.04	

MOBBIO database (visible)

smallest filter	largest filter	Periocular			Iris	Periocular+Iris	
		Proposed (PP)	Gabor (PG)	Fusion PP+PG	IR	Fusion PP+IR	Fusion PG+IR
5	32	14.99	14.92	12.81 (-14.11%)	18.81	11.33 (-39.77%)	11.11 (-40.94%)
5	64	13.01		11.39 (-12.40%)		9.67 (-48.58%)	
10	64	**11.96**		**10.98** (-8.22%)		9.71 (-48.37%)	

TABLE I

VERIFICATION RESULTS IN TERMS OF EER. THE BEST CASE OF EACH COLUMN IS MARKED IN BOLD. FUSION RESULTS: THE RELATIVE EER VARIATION WITH RESPECT TO THE BEST INDIVIDUAL SYSTEM IS GIVEN IN BRACKETS (ONLY WHEN THERE IS PERFORMANCE IMPROVEMENT).

in visible light with a webcam. One advantage of periocular systems is that existing setups of face and iris can be used for recognition purposes.

We carry out experiments for different range of radii of the ring-shaped areas, which are set in proportion to the average radius of the pupil and sclera boundaries of the databases (as given by available groundtruth). All the configurations tested with the NIR database have similar performance, and only when the top-end of the range of radii is made large in comparison with the iris size, a worsening in performance is observed. On the other hand, the best configuration with the visible database is the one covering as much as twice the average sclera radius. In absolute terms, the optimum range is very similar for both databases, despite differences in image size. This is good, since making iris images larger does not imply making the extraction filters bigger, with significant implications in computational time savings.

The system proposed here is also compared with another periocular system based on Gabor filters, as well as with an iris texture matcher. It is observed that each periocular system works better with one particular database, but the fusion of both systems results in a significant improvement for both databases (up to 14% of improvement in the EER). As regards the iris matcher, it works considerably better than the periocular systems with NIR data, while the opposite behavior is observed with visible data. Despite the poorer performance with the webcam database, however, fusing the iris matcher with any of the two periocular systems leads to EER improvements of more than 40%.

Most studies of periocular recognition have not focused on detection of the periocular region (it is manually extracted) but on feature extraction only. Only Park *et al*. [2] used a Viola-Jones face detector [39] plus heuristics measurements (not specified) to extract the periocular region, so successful extraction relied on an accurate detection of the whole face. In this initial work, we have proposed and evaluated the feasibility of local symmetry patterns for periocular recognition purposes. Our future work will include incorporating automatic detection of the periocular region [9] to the developments proposed here, as well as incorporating other periocular approaches to our comparison [1]. The use of visible images of higher resolution is also another avenue of study, as well as the use of full-face images.

ACKNOWLEDGMENT

Author A. M. thanks the EU BBfor2 project for funding his doctoral research. Author F. A.-F. thanks the Swedish Research Council and the EU for for funding his postdoctoral research. Authors acknowledge the CAISR program of the Swedish Knowledge Foundation and the EU COST Action IC1106. Authors also thank the Biometric Recognition Group (ATVS-UAM) for making the iris BioSec database available.

REFERENCES

[1] G. Santos and H. Proenca, "Periocular biometrics: An emerging technology for unconstrained scenarios," in *Proc. IEEE Workshop on Computational Intelligence in Biometrics and Identity Management (CIBIM)*, April 2013, pp. 14–21.

[2] U. Park, R. R. Jillela, A. Ross, and A. K. Jain, "Periocular biometrics in the visible spectrum," *IEEE Transactions on Information Forensics and Security*, vol. 6, no. 1, pp. 96–106, 2011.

[3] K. Hollingsworth, S. S. Darnell, P. E. Miller, D. L. Woodard, K. W. Bowyer, and P. J. Flynn, "Human and machine performance on periocular biometrics under near-infrared light and visible light," *IEEE Transactions on Information Forensics and Security*, vol. 7, no. 2, pp. 588–601, 2012.

[4] F. Smeraldi and J. Bigün, "Retinal vision applied to facial features detection and face authentication," *Pattern Recognition Letters*, vol. 23, no. 4, pp. 463–475, 2002.

[5] S. Li and A. Jain, Eds., *Handbook of Face Recognition*. Springer Verlag, 2004.

[6] K. Bowyer, K. Hollingsworth, and P. Flynn, "Image understanding for iris biometrics: a survey," *Computer Vision and Image Understanding*, vol. 110, pp. 281–307, 2007.

[7] P. E. Miller, J. R. Lyle, S. J. Pundlik, and D. L. Woodard, "Performance evaluation of local appearance based periocular recognition," *Proc. IEEE Int. Conf. on Biometrics: Theory, Applications, and Systems, BTAS*, 2010.

[8] D. Woodard, S. Pundlik, P. Miller, R. Jillela, and A. Ross, "On the fusion of periocular and iris biometrics in non-ideal imagery," *Proc. IAPR International Conference on Pattern Recognition, ICPR*, 2010.

[9] F. Alonso-Fernandez and J. Bigun, "Eye detection by complex filtering for periocular recognition," *Proc. 2nd International Workshop on Biometrics and Forensics, IWBF, Valletta, Malta*, 2014.

[10] J. Daugman, "How iris recognition works," *IEEE Trans. on Circuits and Systems for Video Technology*, vol. 14, pp. 21–30, 2004.

[11] T. Ojala, M. Pietikainen, and T. Maenpaa, "Multiresolution gray-scale and rotation invariant texture classification with local binary patterns," *IEEE Trans. on Pattern Analysis and Machine Intelligence*, vol. 24, no. 7, pp. 971–987, 2002.

[12] N. Dalal and B. Triggs, "Histograms of oriented gradients for human detection," *Proc. IEEE Conference on Computer Vision and Pattern Recognition, CVPR*, 2005.

[13] D. Lowe, "Distinctive image features from scale-invariant key points," *International Journal of Computer Vision*, vol. 60, no. 2, pp. 91–110, 2004.

[14] P. E. Miller, A. W. Rawls, S. J. Pundlik, and D. L. Woodard, "Personal identification using periocular skin texture," *Proc. ACM Symposium on Applied Computing (SAC), Sierre, Switzerland, March 22-26, 2010*, pp. 1496–1500, 2010.

[15] D. L. Woodard, S. J. Pundlik, J. R. Lyle, and P. E. Miller, "Periocular region appearance cues for biometric identification," *Proc. IEEE Computer Vision and Pattern Recognition Biometrics Workshop*, 2010.

[16] F. Alonso-Fernandez and J. Bigun, "Periocular recognition using retinotopic sampling and gabor decomposition," *Proc. Intl Workshop What's in a Face? WIAF, in conjunction with the European Conference on Computer Vision, ECCV*, vol. Springer LNCS-7584, pp. 309–318, 2012.

[17] S. Bharadwaj, H. S. Bhatt, M. Vatsa, and R. Singh, "Periocular biometrics: When iris recognition fails," *Proc. IEEE Conference on Biometrics: Theory, Applications and Systems, BTAS*, 2010.

[18] F. Juefei-Xu, M. Cha, J. Heyman, S. Venugopalan, R. Abiantun, and M. Savvides, "Robust local binary pattern feature sets for periocular biometric identification," *Proc. IEEE Conference on Biometrics: Theory, Applications and Systems, BTAS*, 2010.

[19] F. Juefei-Xu, K. Luu, M. Savvides, T. Bui, and C. Suen, "Investigating age invariant face recognition based on periocular biometrics," *Proc. Intl Joint Conference on Biometrics, IJCB*, 2011.

[20] T. Beer, "Walsh transforms," *American Journal of Physics*, vol. 49, no. 5, 1981.

[21] K. I. Laws, "Rapid texture identification," pp. 376–381, 1980. [Online]. Available: http://dx.doi.org/10.1117/12.959169

[22] N. Ahmed, T. Natarajan, and K. Rao, "Discrete cosine transform," *Computers, IEEE Transactions on*, vol. C-23, no. 1, pp. 90–93, Jan 1974.

[23] S. Mallat, "A theory for multiresolution signal decomposition: the wavelet representation," *Pattern Analysis and Machine Intelligence, IEEE Transactions on*, vol. 11, no. 7, pp. 674–693, Jul 1989.

[24] D. Hurley, M. Nixon, and J. Carter, "A new force field transform for ear and face recognition," in *Image Processing, 2000. Proceedings. 2000 International Conference on*, vol. 1, 2000, pp. 25–28 vol.1.

[25] H. Bay, A. Ess, T. Tuytelaars, and L. V. Gool, "Speeded-up robust features (surf)," *Computer Vision and Image Understanding*, vol. 110, no. 3, pp. 346 – 359, 2008, similarity Matching in Computer Vision and Multimedia. [Online]. Available: http://www.sciencedirect.com/science/article/pii/S1077314207001555

[26] D. Clausi and M. Jernigan, "Towards a novel approach for texture segmentation of sar sea ice imagery," in *26th International Symposium on Remote Sensing of Environment and 18th Annual Symposium of the Canadian Remote Sensing Society, Vancouver, BC, Canada*, 1996, p. 257261.

[27] A. Mikaelyan and J. Bigun, "Symmetry assessment by finite expansion: Application to forensic fingerprints," *Proc. International Conference of the Biometrics Special Interest Group, BIOSIG, Darmstadt, Germany*, 2014.

[28] J. Bigun and G. Granlund, "Optimal orientation detection of linear symmetry," *Proc. 1st International Conference on Computer Vision, ICCV*, pp. 433–438, June 1987.

[29] J. Bigun, T. Bigun, and K. Nilsson, "Recognition by symmetry derivatives and the generalized structure tensor," *IEEE Trans. on Pattern Analysis and Machine Intelligence*, vol. 26, pp. 1590–1605, 2004.

[30] J. Bigun, "Pattern recognition in images by symmetry and coordinate transformation," *Computer Vision and Image Understanding*, vol. 68, no. 3, pp. 290–307, 1997.

[31] J. Bigun, *Vision with Direction*. Springer, 2006.

[32] A. Gilperez, F. Alonso-Fernandez, S. Pecharroman, J. Fierrez, and J. Ortega-Garcia, "Off-line signature verification using contour features," *Proc. International Conference on Frontiers in Handwriting Recognition, ICFHR*, 2008.

[33] L. Masek, "Recognition of human iris patterns for biometric identification," Master's thesis, School of Computer Science and Software Engineering, University of Western Australia, 2003.

[34] H. Hofbauer, F. Alonso-Fernandez, P. Wild, J. Bigun, and A. Uhl, "A ground truth for iris segmentation," *Proc. International Conference on Pattern Recognition, ICPR*, 2014.

[35] J. Fierrez, J. Ortega-Garcia, D. Torre-Toledano, and J. Gonzalez-Rodriguez, "BioSec baseline corpus: A multimodal biometric database," *Pattern Recognition*, vol. 40, no. 4, pp. 1389–1392, April 2007.

[36] A. F. Sequeira, J. ao C. Monteiro, A. Rebelo, and H. P. Oliveira, "Mobbio: a multimodal database captured with a portable handheld device," *Proc International Conference on Computer Vision Theory and Applications, VISAPP*, vol. 3, pp. 133–139, 2014.

[37] A. Jain, K. Nandakumar, and A. Ross, "Score Normalization in Multimodal Biometric Systems," *Pattern Recognition*, vol. 38, no. 12, pp. 2270–2285, December 2005.

[38] E. Bigun, J. Bigun, B. Duc, and S. Fischer, "Expert Conciliation for Multi Modal Person Authentication Systems by Bayesian Statistics," *Proc. International Conference on Audio- and Video-Based Biometric Person Authentication, AVBPA*, vol. Springer LNCS-1206, pp. 291–300, 1997.

[39] P. Viola and M. Jones, "Rapid object detection using a boosted cascade of simple features," *Proc. Computer Vision and Pattern Recognition Conference, CVPR*, vol. 1, pp. 511–518, 2001.